IOP Publishing New J. Phys. 26 (2024) 103043 https://doi.org/10.1088/1367-2630/ad8954

New Journal of Physics
The open access journal at the forefront of physics

Deutsche Physikalische Gesellschaft DPG
IOP Institute of Physics

Published in partnership with: Deutsche Physikalische Gesellschaft and the Institute of Physics

OPEN ACCESS

RECEIVED
10 May 2024

REVISED
21 September 2024

ACCEPTED FOR PUBLICATION
21 October 2024

PUBLISHED
1 November 2024

PAPER

High-fidelity remote entanglement between superconducting fixed-frequency qubits

Mari Ohfuchi* and **Shintaro Sato**

Quantum Laboratory, Fujitsu Research, Fujitsu Limited, Atsugi 243-0197, Japan
* Author to whom any correspondence should be addressed.

E-mail: mari.ohtuti@fujitsu.com

Keywords: superconducting fixed-frequency qubits, quantum interconnects, remote entanglement

Abstract

Highly accurate quantum state transfer and remote entanglement between superconducting fixed-frequency qubits have not yet been realized. In this study, we calculate the characteristics of a transmission path with a 1- or 0.25 m superconducting coaxial cable and use the characteristics to perform time evolution simulations of quantum state transfer and remote entanglement between superconducting fixed-frequency qubits. We find that remote entanglement, or half-quantum state transfer, can achieve a high fidelity $> 99\%$ even in the presence of a qubit frequency detuning caused by manufacturing fluctuations, while a small qubit frequency detuning substantially reduces the efficiency of quantum state transfer. Quantum circuit simulations modeling proposed remote entanglement demonstrate that teleportation of a logical qubit with a 3×3 surface code, as an example of computation using remote entanglement, attains nearly the same fidelity as in-node computation for both 1- and 0.25 m cable lengths.

1. Introduction

Superconducting quantum computer systems are expected to be a platform for practical quantum computing in the future [1, 2]. This requires scaling up of superconducting computers with different levels of modularity and interconnects between them [2–26]. Among them, medium-range quantum interconnects [6–19] are also important to realize non-two-dimensional (non-2D) quantum error-correcting codes [2, 27]. Superconducting qubits separated by 0.1–1 m in a refrigerator are connected primarily through superconducting coaxial cables that pass microwave signals [6–16]. Millimeterwave photonic links [17], or acoustic transmission lines as quantum phononic channels [18, 19], have also been reported. Herein, we focus on interconnects via superconducting coaxial cables.

Recent advances in the fidelity of quantum state transfer through superconducting coaxial cables have been achieved with a scheme using the standing-wave modes of cables [6–9] (figure 1(a)). Half-quantum state transfer corresponds to remote entanglement. For both quantum state transfer and remote entanglement, fidelities of 91% and 99% were reported through 1- and 0.25 m cables, respectively [6, 7]. However, these experimental setups are limited to a combination of frequency-tunable qubits [28–31] and tunable couplers [32]. This can be because, as we discuss later in this paper (figure 3 in section 2.3), small qubit frequency detunings from the standing-wave mode of the cable significantly reduce the transfer efficiency.

Meanwhile, fixed-frequency qubits, typically transmons with a single Josephson junction [33], have several advantages. Low sensitivity to low frequency charge and magnetic-flux fluctuations results in long coherence times [33–41]. The simple circuit structure and small number of wires are advantageous for large-scale integration. Furthermore, two-qubit gates using only microwaves, cross-resonance gates, have been developed [42–52]. No flux control is required, which means no new noise channels are introduced into the system. However, quantum state transfer using cable standing-wave modes in the current scheme may not be applicable to fixed-frequency qubits. Even if the qubits are fabricated at a frequency that matches the standing-wave mode of the cable, slight frequency shifts are unavoidable with the current manufacturing

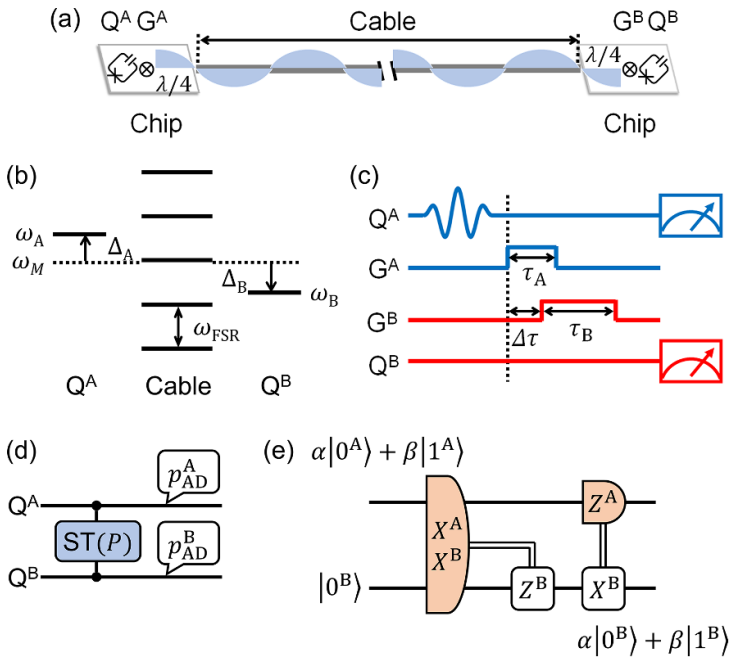

Figure 1. Schematics of this study. (a) Quantum interconnect via a superconducting coaxial cable and coplanar waveguides, where Q^{A} and Q^{B} are superconducting fixed-frequency qubits, G^{A} and G^{B} are tunable couplers, and λ represents the wavelength. (b) Energy diagram (in $\hbar$): ω_{A}, ω_{B}, and ω_M are the frequencies of Q^{A}, Q^{B}, and the Mth standing-wave mode of the transmission path, respectively. The detunings of ω_{A} and ω_{B} measured from ω_M are denoted by Δ_{A} and Δ_{B}, respectively. The free spectral range ω_{FSR} is the equally spaced frequencies of the standing-wave mode. (c) Control sequence for quantum state transfer: τ_{A} and τ_{B} are the durations to turn on G^{A} and G^{B}, respectively, and $\Delta\tau$ is the delay time given to τ_{B}. (d) Quantum circuit model of remote entanglement: ST(P) represents state transfer with a rate of P, and $p^{\mathrm{A}}_{\mathrm{AD}}$ and $p^{\mathrm{B}}_{\mathrm{AD}}$ are error rates for amplitude damping of Q^{A} and Q^{B}, respectively. (e) Quantum circuit of teleportation of a physical qubit. The semi-oval shape represents the measurement.

processes [53, 54]. These qubit frequency detunings can considerably reduce the transfer efficiency as mentioned above. Recently, we proposed remote cross-resonance gates with a high concurrence in the presence of manufacturing fluctuations for quantum state transfer and remote entanglement [55]; however, various approaches should be explored. In this paper, we consider a transmon for a fixed-frequency qubit. We perform time evolution simulations to evaluate quantum state transfer and remote entanglement between frequency-detuned qubits through cable standing-wave modes. Based on these results, we propose a scheme specialized for remote entanglement that can achieve a high fidelity $> 99\%$ even in the presence of a qubit frequency detuning. Furthermore, we perform quantum circuit simulations for teleportation of physical and logical qubits, as examples of computation using remote entanglement. We demonstrate that the proposed remote entanglement, which shows lower fidelity than in-node computation in physical qubit teleportation, can achieve nearly the same fidelity as in-node computation in logical qubit teleportation through ingenuity in qubit arrangements and quantum circuits. The schematics of this study are summarized in figure 1.

The remainder of this paper is organized as follows. In section 2, we calculate the characteristics of transmission paths and use the characteristics to perform time evolution simulations and find the optimized control sequence for quantum state transfer and remote entanglement without or with a qubit frequency detuning. In section 3, a quantum circuit model of remote entanglement is constructed based on the results of time evolution simulations, and quantum circuit simulations are performed to compare the performance of teleportation of physical and logical qubits using remote entanglement with in-node computation. Finally, section 4 presents the conclusions of the study.

2. Quantum state transfer and remote entanglement

We first configure transmission paths and then perform time evolution simulations using the characteristics of the transmission paths to optimize quantum state transfer and remote entanglement without or with a qubit frequency detuning. Finally, we consider the extensibility of remote entanglement operations.

2.1. Transmission paths

The transmission path consists of a superconducting coaxial cable and coplanar waveguides (figure 1(a)). The microwave speeds in the cable and coplanar waveguide are obtained as $v_{\mathrm{Cable}} = 2.472 \times 10^8$ m s^{-1} and $v_{\mathrm{CPW}} = 1.157 \times 10^8$ m s^{-1}, respectively, from experimental results [7]. To minimize the dissipation at the

Table 1. Characteristics of transmission paths: cable length (l_{Cable}), coplanar waveguide length (l_{CPW}), and free spectral range [$\omega_{\mathrm{FSR}}/(2\pi)$] for the standing-wave mode of 5 GHz, where the target cable lengths are 1 (upper half) and 0.25 (lower half) m. Q_m and T_m are Q values and relaxation time for the mth standing-wave mode, respectively.

l_{Cable} (m)	l_{CPW} (mm)	$\omega_{\mathrm{FSR}}/(2\pi)$ (GHz)	m	Q_m ($\times 10^5$)	T_m (μs)
			41	2.90	9.68
			42	2.97	9.69
1.0832	5.8	0.1163	43	3.00	9.55
			44	2.98	9.26
			45	2.91	8.84
			11	1.81	6.80
			12	5.19	17.9
0.2966	5.8	0.3846	13	12.0	38.2
			14	5.65	16.7
			15	2.34	6.45

junction between the cable and the coplanar waveguide, the lengths of the cable and the coplanar waveguide are given as follows:

$$\begin{aligned} l_{\mathrm{Cable}} &= \frac{M-1}{2}\frac{v_{\mathrm{Cable}}}{\omega_M/(2\pi)} = \frac{M-1}{2}\lambda_{\mathrm{Cable}} \\ l_{\mathrm{CPW}} &= \frac{1}{4}\frac{v_{\mathrm{CPW}}}{\omega_M/(2\pi)} = \frac{1}{4}\lambda_{\mathrm{CPW}}, \end{aligned} \tag{1}$$

where λ_{Cable} and λ_{CPW} are the microwave wavelengths in the cable and coplanar waveguide, respectively. The frequency of the Mth standing-wave mode of the transmission path is set to $\omega_M/(2\pi) = 5$ GHz (figure 1(b)). Let the target cable lengths be 1 and 0.25 m. We obtain $M = 43$ for the target cable lengths of 1 m and $M = 13$ for 0.25 m so that the cable length is close to the target cable length.

Then, we consider two upper and lower standing-wave modes centered on M (figure 1(b)), that is, $m = M,\ M \pm 1,\ M \pm 2$. The mode spacing, namely, free spectral range, is obtained as $\omega_{\mathrm{FSR}} = \omega_M/M$, and $\omega_m = m\omega_{\mathrm{FSR}}$. As the number of cable modes increases, the obtained fidelity decreases; however, when the number of modes exceeds five, the change becomes small even for a 1 m cable. The Q value of the mth standing-wave mode for the junction Q^m_{Loss} is given by:

$$\begin{aligned} Q^m_{\mathrm{Loss}} &= \frac{\omega_m L}{\cos^2(2\pi\, l_{\mathrm{CPW}}/\lambda^m_{\mathrm{CPW}})\, R} \\ L &\approx \frac{1}{2}\left(2\mathcal{L}_{\mathrm{CPW}} l_{\mathrm{CPW}} + \mathcal{L}_{\mathrm{Cable}} l_{\mathrm{Cable}}\right), \end{aligned} \tag{2}$$

where $\lambda^m_{\mathrm{CPW}} = 2\pi v_{\mathrm{CPW}}/\omega_m$ is the wavelength of the mth mode in the coplanar waveguide. The specific inductances of the coplanar wave guide and coaxial cable, $\mathcal{L}_{\mathrm{CPW}} = 402$ nH m^{-1} and $\mathcal{L}_{\mathrm{Cable}} = 216$ nH m^{-1}, and the resistance between the coplanar waveguide and coaxial cable, $R = 0.0749\mathrm{n}\Omega$, are obtained from experimental results [7]. The Q value of the mth standing-wave mode Q_m is given as follows:

$$1/Q_m = 1/Q_{\mathrm{Cable}} + 1/Q^m_{\mathrm{Loss}}, \tag{3}$$

where Q_{Cable} is the cable-specific value, which is obtained as 1.2×10^6 for a 0.25 m coaxial cable [7]. The relation $Q_m = \omega_m T_m$ gives the relaxation time of the mth mode T_m. For each cable length, Q_m and T_m are summarized in table 1 with other characteristics of transmission paths.

2.2. Time evolution simulations

Two fixed-frequency qubits Q^{A} and Q^{B} are connected by the transmission path through tunable couplers G^{A} and G^{B}, as shown in figure 1(a). The qubit frequency detunings measured from ω_M and annihilation operators for Q^{A} and Q^{B} are denoted by Δ_{A} and Δ_{B} and σ_{A} and σ_{B}, respectively. The frequency and annihilation operator for the mth standing-wave mode are represented by $\omega_m = m\omega_{\mathrm{FSR}}$ and σ_m, respectively. The Hamiltonian for quantum state transfer and remote entanglement can be written as follows:

$$H/\hbar = \Delta_{\mathrm{A}}\sigma_{\mathrm{A}}^{\dagger}\sigma_{\mathrm{A}} + \Delta_{\mathrm{B}}\sigma_{\mathrm{B}}^{\dagger}\sigma_{\mathrm{B}} + \sum_{m=M-2}^{M+2}(m-M)\,\omega_{\mathrm{FSR}}\sigma_m^{\dagger}\sigma_m + \sum_{m=M-2}^{M+2} g_{\mathrm{A}}\sqrt{\omega_m/\omega_M}\left(\sigma_{\mathrm{A}}\sigma_m^{\dagger} + \sigma_A^{\dagger}\sigma_m\right) + \sum_{m=M-2}^{M+2}(-1)^m g_{\mathrm{B}}\sqrt{\omega_m/\omega_M}\left(\sigma_{\mathrm{B}}\sigma_m^{\dagger} + \sigma_B^{\dagger}\sigma_m\right), \quad (4)$$

where g_{A} and g_{B} are the coupling between the qubits and the Mth mode. Notably, in multimode coupling, the coupling is proportional to the square root of the frequency [6, 56]. When G^{A} and G^{B} are on, couplings are adjusted to $g_{\mathrm{A}}/(2\pi) = g_{\mathrm{B}}/(2\pi) = 5$ MHz.

We numerically simulate time evolution for the Hamiltonian in equation (4) using the QuTip framework [57, 58]. When dissipation is not considered, the time evolution is solved using the state vector. The time evolution with dissipation is investigated by solving the Lindblad master equation using the density matrix ρ. The Lindblad master equation is given as follows:

$$\dot{\rho}(t) = -\frac{i}{\hbar}\left[H(t), \rho(t)\right] + \sum_n \frac{\gamma_n}{2}\left[2L_n\rho(t)L_n^{\dagger} - \rho(t)L_n^{\dagger}L_n - L_n^{\dagger}L_n\rho(t)\right], \quad (5)$$

where t is time, L_n are the operators to couple to the environment, and γ_n are their rates. A typical relaxation time $T_1 = 100$ μs is used for fixed-frequency qubits in this section. The relaxation times of each mode of the transmission path T_m are given in table 1.

2.3. Quantum state transfer

We start with quantum state transfer in the absence of a qubit frequency detuning. As shown in the control sequence (figure 1(c)), after preparing Q^{A} to $|1\rangle$, the state $|1\rangle$ is transferred to Q^{B} by turning on G^{A} and G^{B} during τ_{A} and τ_{B}, respectively, and τ_{B} is delayed by $\Delta\tau$. By expressing the qubit state as $|\Phi\rangle = c_{00}|00\rangle + c_{01}|01\rangle + c_{10}|10\rangle + c_{11}|11\rangle$, where each ket represents the eigenstate of H in order of $Q^{\mathrm{A}}Q^{\mathrm{B}}$, the ideal initial and final qubit states for quantum state transfer can be written as $|\Phi^{\mathrm{I}}\rangle = |10\rangle$ and $|\Phi_{\mathrm{ST}}^{\mathrm{F}}\rangle = |01\rangle$, respectively. We perform time evolution simulations to extensively search for the maximum final state fidelity $\mathcal{F}_{\mathrm{ST}}$ with respect to the combination of τ_{A}, τ_{B}, and $\Delta\tau$ in the control sequence, where $\mathcal{F}_{\mathrm{ST}} = \left|\langle\Phi|\Phi_{\mathrm{ST}}^{\mathrm{F}}\rangle\right|^2$.

The results of the time evolution simulations with the initial qubit state of $|\Phi^{\mathrm{I}}\rangle$ for a 1 m coaxial cable are presented in figure 2. For each $\Delta\tau$, the maximum $\mathcal{F}_{\mathrm{ST}}$ is searched in steps of 0.1 ns for τ_{A} and τ_{B}. The search range for τ_{A} and τ_{B} ranges from 0.0 to 80.0 ns. A longer duration returns the state $|1\rangle$ to Q^{A}. The maximum $\mathcal{F}_{\mathrm{ST}}$ without dissipation is shown in figure 2(a) (blue solid curve). The total control sequence duration $\tau = \Delta\tau + \tau_{\mathrm{B}}$ at the $\mathcal{F}_{\mathrm{ST}}$ value as well as τ_{A} and τ_{B} are given in figure 2(b). Hereafter, it is not explicitly mentioned that the plotted data are those at the maximum fidelity for each $\Delta\tau$. The first and second maximum $\mathcal{F}_{\mathrm{ST}}$ values with respect to $\Delta\tau$ are found at $\Delta\tau = 0.0$ and 23.0 ns, respectively. The $\mathcal{F}_{\mathrm{ST}}$ values are 99.43% and 99.66%, and the second maximum is larger than the first one. For larger $\Delta\tau$, oscillations of approximately 9 ns are observed, which appears to correspond to $\omega_{\mathrm{FSR}}/(2\pi) = 0.1163$ GHz. We find that the decrease of $|01\rangle$ mainly occupies the $(M \pm 1)$th modes of the transmission path.

When dissipation is considered (red-dotted curve in figure 2(a)), both first and second maximum $\mathcal{F}_{\mathrm{ST}}$ values reduce to 99.19% and 99.34%, respectively, where $\mathcal{F}_{\mathrm{ST}} = \langle\Phi_{\mathrm{ST}}^{\mathrm{F}}|\rho|\Phi_{\mathrm{ST}}^{\mathrm{F}}\rangle$. The second maximum value is still larger than the first one, despite a longer control sequence duration. We find that $\mathcal{F}_{\mathrm{ST}}$ without a qubit frequency detuning can exceed 99% around $\Delta\tau = 0.0$ and 23.0 ns even for a 1 m cable.

Similar results are obtained for a 0.25 m coaxial cable (appendix A, figure 9). When dissipation is not considered, the first and second maximum $\mathcal{F}_{\mathrm{ST}}$ values are 99.96% and 99.97% at $\Delta\tau = 0.0$ and 15.0 ns, respectively. The second maximum is slightly larger than the first one. Oscillations of approximately 2.5 ns for large $\Delta\tau$ correspond to $\omega_{\mathrm{FSR}}/(2\pi) = 0.3846$ GHz. Both first and second maximum $\mathcal{F}_{\mathrm{ST}}$ values with dissipation reduce to 99.86%. The second maximum value becomes equal with the first one, with the larger control sequence duration. The higher fidelity than the 1 m cable is considered due to the larger ω_{FSR} because the decay of fidelity is caused by the existence of the $(M \pm 1)$ modes of the transmission path.

Then, we consider a qubit frequency detuning $\Delta/(2\pi)$ of 5 MHz. A standard deviation of the frequency distribution of 14 MHz has already been achieved with the current technology [53, 54]. The frequency shift of 5 MHz corresponds to 0.1% of the qubit frequency ~5 GHz and is the standard deviation of the frequency distribution that is required to achieve a 1000-qubit computer. For each $\Delta\tau$ in addition to τ_{A} and τ_{B}, $\Delta_{\mathrm{A}}/(2\pi)$ is also searched in the range of -6.0 to 1.0 MHz in steps of 0.1 MHz, where $\Delta_{\mathrm{B}} - \Delta_{\mathrm{A}} = \Delta = 2\pi \cdot 5$ MHz. Results of the time evolution simulations with the initial state of $|\Phi^{\mathrm{I}}\rangle$ for a 1 m coaxial cable are shown in figure 3. A detuning of 5 MHz considerably reduces $\mathcal{F}_{\mathrm{ST}}$. The maximum $\mathcal{F}_{\mathrm{ST}}$ value is 88.36% at $\Delta\tau = 45.0$ ns. As $\Delta\tau$ increases, $\mathcal{F}_{\mathrm{ST}}$ increases; however, $\mathcal{F}_{\mathrm{ST}}$ does not further increase because $\Delta\tau$ exceeds τ_{A}. The qubit frequency detuning $\Delta_{\mathrm{A}}/(2\pi)$ varies from -3.1 MHz to -2.4 MHz, which means that high

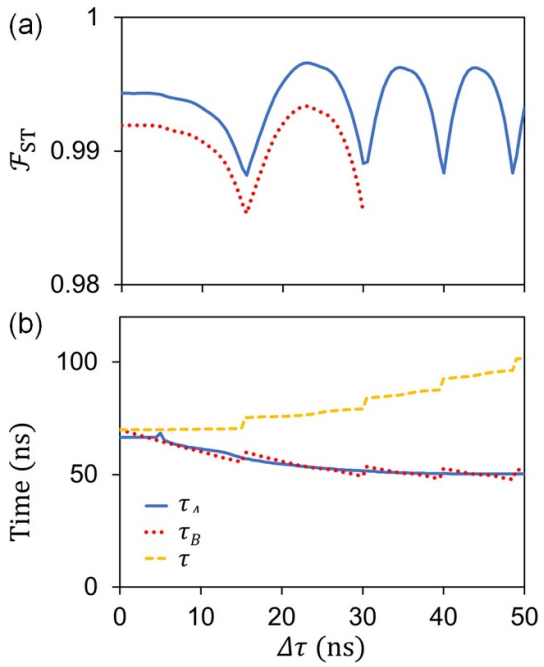

Figure 2. Results of time evolution simulations of quantum state transfer without a qubit frequency detuning for a 1 m coaxial cable. (a) Maximum state fidelity $\mathcal{F}_{ST}$ for each $\Delta\tau$: the blue solid and red-dotted curves are the results without and with dissipation, respectively. (b) Control sequence parameters of τ_A, τ_B, and τ giving the $\mathcal{F}_{ST}$ value without dissipation in (a). The first and second maximum $\mathcal{F}_{ST}$ (%) and the control sequence parameters $\Delta\tau$, τ_A, and τ (ns) are summarized as $\{\mathcal{F}_{ST}, \Delta\tau, \tau_A, \tau\} = \{99.43, 0.0, 66.6, 69.9\}$ and $\{99.66, 23.0, 53.5, 76.5\}$ without dissipation and $\{99.19, 0.0, 66.6, 69.9\}$ and $\{99.34, 22.8, 53.6, 76.4\}$ with dissipation, respectively.

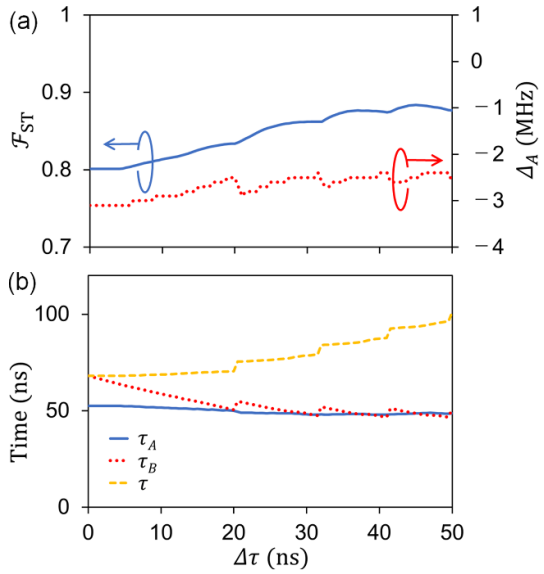

Figure 3. Results of time evolution simulations of quantum state transfer with a qubit frequency detuning of 5 MHz for a 1 m coaxial cable in the absence of dissipation. (a) Maximum state fidelity $\mathcal{F}_{ST}$ and qubit frequency detuning Δ_A for each $\Delta\tau$. (b) Control sequence parameters of τ_A, τ_B, and τ giving the $\mathcal{F}_{ST}$ value. The maximum $\mathcal{F}_{ST}$ (%), the control sequence parameters $\Delta\tau$, τ_A, and τ (ns), and $\Delta_A/(2\pi)$ (MHz) are summarized as $\{\mathcal{F}_{ST}, \Delta\tau, \tau_A, \tau, \Delta_A/(2\pi)\} = \{88.36, 45.0, 48.6, 93.6, -2.5\}$.

fidelity is obtained when the standing-wave mode is near the center for the qubit frequency detuning of 5 MHz. Since $\mathcal{F}_{ST}$ is quite small, the simulation considering the dissipation is not performed.

For a 0.25 m cable, $\mathcal{F}_{ST}$ remains small at 88.56% (appendix A, figure 10) because the decay of fidelity is caused by the qubit frequency detunings from the Mth mode of the transmission path and is not related to ω_{FSR}. As mentioned in the introduction, a small qubit frequency detuning of 5 MHz substantially reduces the transfer efficiency.

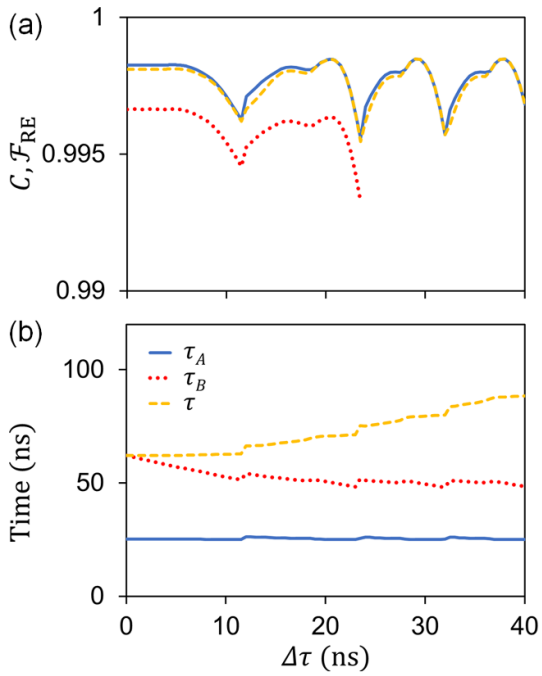

Figure 4. Results of time evolution simulations of remote entanglement without a qubit frequency detuning for a 1 m coaxial cable. (a) Maximum concurrence C and state fidelity $\mathcal{F}_{RE}$ for each $\Delta\tau$: the orange-dashed, blue solid, and red-dotted curves are C and $\mathcal{F}_{RE}$ without and with dissipation, respectively. (b) Control sequence parameters of τ_A, τ_B, and τ giving the $\mathcal{F}_{RE}$ value without dissipation in (a). The first and second maximum $\mathcal{F}_{RE}$ (%) and the control sequence parameters $\Delta\tau$, τ_A, and τ (ns) are summarized as $\{\mathcal{F}_{RE}, \Delta\tau, \tau_A, \tau\} = \{99.83, 4.8, 25.4, 62.1\}$ and $\{99.85, 20.5, 25.0, 70.8\}$ without dissipation and $\{99.67, 4.6, 25.3, 62.1\}$ and $\{99.64, 20.4, 25.0, 70.7\}$ with dissipation.

2.4. Remote entanglement

Herein, we consider remote entanglement, that is, half-quantum state transfer. After preparing Q_A to $|1\rangle$, the half of state $|1\rangle$ is transferred to Q_B by turning on G_A and G_B, where τ_A is roughly halved compared with full quantum state transfer in the previous section. The ideal initial and final qubit states for remote entanglement can be written as $|\Phi^I\rangle = |10\rangle$ and $|\Phi^F_{RE}\rangle = (|10\rangle + |01\rangle)/\sqrt{2}$, respectively. Once such an entangled state is generated, it can be changed to an arbitrary Bell state by applying local gates. Time evolution simulations are performed again to extensively search for the maximum final state fidelity $\mathcal{F}_{RE}$ with respect to the combination of τ_A, τ_B, and $\Delta\tau$ in the control sequence, where $\mathcal{F}_{RE} = |\langle\Phi|\Phi^F_{RE}\rangle|^2$. Results of the time evolution simulations with the initial state of $|\Phi^I\rangle$ for a 1 m coaxial cable are presented in figure 4. In the absence of dissipation, the concurrence given as follows:

$$C = 2|c_{10}||c_{01}| \tag{6}$$

is a useful measure of the strength of entanglement [59], which is defined so that C becomes 1 when $\Phi = \Phi^F_{RE}$. Figure 4(a) shows C without dissipation (orange-dashed curve). The first and second maximum values of C are found to be 99.81% and 99.85% at $\Delta\tau = 4.8$ and 20.5 ns, respectively. We find that $\mathcal{F}_{RE}$ without dissipation (blue solid curve) is approximately along C, which means that the phase of the qubit $|01\rangle$ state relative to the $|01\rangle$ state does not change during the state transfer. The first and second maximum $\mathcal{F}_{RE}$ values are 99.83% and 99.85% without dissipation, respectively. For $\mathcal{F}_{RE}$ with dissipation (red-dotted curve), the first and second maximum values are 99.67% and 99.64%, respectively, where $\mathcal{F}_{RE} = \langle\Phi^F_{RE}|\rho|\Phi^F_{RE}\rangle$. The second maximum without dissipation is slightly larger than the first one; however, the relationship is reversed with dissipation.

Similar results are obtained for a 0.25 m coaxial cable (appendix A, figure 11). The first and second maximum values of C are found to be 99.98% at $\Delta\tau = 1.0$ and 6.1 ns, respectively. Both the first and second maximum $\mathcal{F}_{RE}$ values are as high as 99.98% without dissipation and 99.90% with dissipation.

We consider a qubit frequency detuning of 5 MHz in the same way as quantum state transfer in the previous section. The results of time evolution simulations with the initial state of $|\Phi^I\rangle$ for a 1 m coaxial cable are presented in figure 5. As shown in figure 5(a), C in the absence of dissipation (orange-dashed curve) has a quite large maximum value of 99.61% at $\Delta\tau = 14.3$ ns. However, the $\mathcal{F}_{RE}$ values immediately after the half-quantum state transfer are less than 0.5 and do not behave in the same way as C (not shown in the figure). The phase of the qubit $|01\rangle$ state relative to the $|10\rangle$ state changes during the state transfer because of

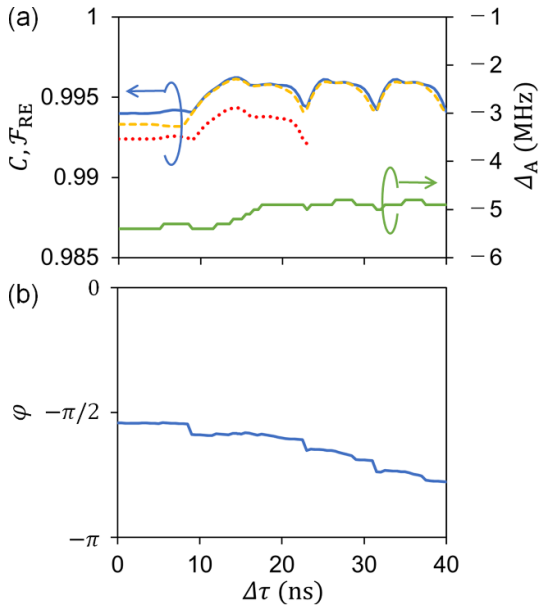

Figure 5. Results of time evolution simulations of remote entanglement with a qubit frequency detuning of 5 MHz for a 1 m coaxial cable. (a) Maximum concurrence C (orange-dashed curve) and state fidelity $\mathcal{F}_{\mathrm{RE}}$ without (blue solid curve) and with (red-dotted curve) dissipation for each $\Delta\tau$. The green solid curve represents the frequency detuning Δ_{A} for $\mathcal{F}_{\mathrm{RE}}$ without dissipation. (b) Phase angle φ of the qubit $|01\rangle$ state relative to the $|10\rangle$ state for $\mathcal{F}_{\mathrm{RE}}$ without dissipation. The maximum $\mathcal{F}_{\mathrm{RE}}$ (%) and control sequence parameters $\Delta\tau$, τ_{A}, and τ (ns), $\Delta_{\mathrm{A}}/(2\pi)$ (MHz), and θ for $R_z(\theta)$ are summarized as $\{\mathcal{F}_{\mathrm{RE}}, \Delta\tau, \tau_{\mathrm{A}}, \tau, \Delta_{\mathrm{A}}/(2\pi), \theta\} = \{99.62, 14.3, 26.7, 66.7, -5.2, 0.58\pi\}$ without dissipation and $\{99.44, 14.3, 26.7, 66.7, -5.2, 0.58\pi\}$ with dissipation.

the qubit frequency detunings. Let the qubit state immediately after the half-quantum state transfer be

$$|\Phi\rangle = |c_{10}||10\rangle + \mathrm{e}^{\mathrm{i}\varphi}\,|c_{01}||01\rangle. \tag{7}$$

The change in the phase angle φ with respect to $\Delta\tau$ is presented in figure 5(b). By performing a local rotation gate $R_z(\theta = -\varphi)$ on Q^{B} after the half-quantum state transfer, $\mathcal{F}_{\mathrm{RE}}$ without dissipation (blue solid curve) becomes aligned with C, as shown in figure 5(a). Since $R_z(\theta)$ can be executed as a virtual gate and the gate time is very short, the increase in error due to $R_z(\theta)$ need not be considered.

The maximum $\mathcal{F}_{\mathrm{RE}}$ value without dissipation is 99.62% at $\Delta\tau = 14.3$ ns and $\theta = 0.58\pi$. This is in sharp contrast to quantum state transfer where a qubit frequency detuning of 5 MHz substantially reduces the maximum $\mathcal{F}_{\mathrm{ST}}$ value to 88.36%. The qubit frequency detuning $\Delta_{\mathrm{A}}/(2\pi)$ varies from -5.4 to -4.8 MHz, which means that ω_{A} is far from the standing-wave mode of the transmission path, whereas ω_{B} is nearly in line with the standing-wave mode. This asymmetric relationship is also very different from quantum state transfer where a high fidelity is obtained when the standing-wave mode is near the center for the qubit frequency detuning of 5 MHz. When dissipation is considered, the maximum $\mathcal{F}_{\mathrm{RE}}$ value reduces to 99.44%, which is still higher than 99%. The difference in fidelity between remote entanglement and full state transfer can be understood as follows. The maximum transfer efficiency between two modes decreases from 100% with increasing detuning. However, we can transfer 50% of the state by calibrating the duration. For remote entanglement, matching a cable mode to the frequency of one qubit allows all 50% of the state, which has been transferred from the other qubit, to be transferred. For full state transfer, 100% of the state cannot be transferred because one of the two couplings must be detuned.

For a 0.25 m coaxial cable (appendix A, figure 12), $\mathcal{F}_{\mathrm{RE}}$ is as high as 99.96% without dissipation and 99.88% with dissipation, and $\Delta_{\mathrm{A}}/(2\pi)$ and θ are -5.7 MHz and 0.56π for the first maximum and -5.4 MHz and 0.57π for the second maximum, respectively. In the case of remote entanglement, even with a frequency detuning between qubits, we can well tune the parameters including the relation with the standing-wave mode of the transmission path (Δ_{A}) and the local rotation gate angle (θ) and obtain a very high fidelity comparable to the fidelity without a qubit frequency detuning.

2.5. Extensibility of remote entanglement

So far, we have fixed the Mth standing-wave mode of the transmission path to 5 GHz and searched an optimal Δ_{A} while keeping a qubit frequency detuning of 5 MHz. However, in practice, we do not know Δ_{A} until we measure the qubit frequencies after fabrication. Here, we first consider what range of Δ_{A} is allowed

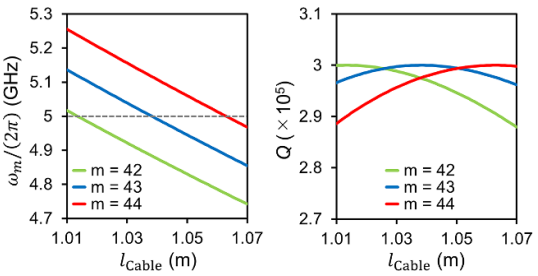

Figure 6. Relationship between the cable length l_{Cable} and the frequency ω_m and Q value of the standing-wave mode for a 1 m coaxial cable.

to achieve remote entanglement with a fidelity $> 99\%$, which is used as a measure of the fidelity for remote entanglement to achieve nearly the same fidelity as in-node computation for teleportation of a logical qubit described in the next section. Further time evolution simulations of remote entanglement for a 1 m cable reveal that $\mathcal{F}_{\mathrm{RE}} > 99\%$ are obtained with $-6.3\ \mathrm{MHz} \geq \Delta_{\mathrm{A}}/(2\pi) \geq -4.1\ \mathrm{MHz}$. This corresponds to $-1.3\ \mathrm{MHz} \geq \Delta_{\mathrm{B}}/(2\pi) \geq 0.9\ \mathrm{MHz}$, which means that either qubit frequency must be within $\pm \sim 1$ MHz of the standing-wave mode for $\mathcal{F}_{\mathrm{RE}} > 99\%$. The other qubit frequency can be either higher or lower than the standing-wave mode. This finding can also explain the lack of high fidelity in full quantum state transfer with a qubit frequency detuning of 5 MHz.

When neither qubit frequency is in the range of $\pm \sim 1$ MHz of the standing-wave mode, the standing-wave mode of the transmission path can be adjusted after qubit fabrications. Figure 6 shows the relationship between the cable length and the frequency and Q value of the standing-wave mode for a 1 m coaxial cable. The frequency of the standing-wave mode continuously changes with the cable length. When the cable length increases or decreases by ∼25 mm, the frequency of the adjacent mode appears around 5 GHz, and the Q value of the adjacent mode becomes maximum. This means that the adjacent mode can be used for state transfer in the same way. The cable length can be adjusted around the lengths where the standing-wave modes appear around 5 GHz. For a 1 m coaxial cable, to increase the standing-wave mode frequency by 5 MHz from 5 GHz, the cable should be shortened by 1 mm from the design length, and conversely, to decrease by 5 MHz, the cable should be lengthened by 1 mm.

Next, we consider a qubit frequency detuning of 10 MHz. Time evolution simulations with dissipation for $\Delta/(2\pi) = 10$ MHz show that the maximum $\mathcal{F}_{\mathrm{RE}}$ (%) and the control sequence parameters (ns), $\Delta_{\mathrm{A}}/(2\pi)$ (MHz), and θ are $\{\mathcal{F}_{\mathrm{RE}}, \Delta\tau, \tau_{\mathrm{A}}, \tau, \Delta_{\mathrm{A}}/(2\pi), \theta\} = \{99.38, 29.8, 76.9, 66.7, -9.8, 0.68\pi\}$ for a 1 m cable and $\{99.80, 30.9, 30.3, 80.9, -9.8, 0.60\pi\}$ for a 0.25 m cable. We find that $\mathcal{F}_{\mathrm{RE}}$ for $\Delta/(2\pi) = 10$ MHz are comparable to those for $\Delta/(2\pi) = 5$ MHz and one qubit frequency detuning $\Delta_{\mathrm{B}}/(2\pi) = 0.2$ MHz is within $\pm \sim 1$ MHz.

These results show the high adjustment capability in remote entanglement operations. Thus, we propose a scheme specialized for remote entanglement that can achieve a high fidelity $> 99\%$ even in the presence of a qubit frequency detuning of 10 MHz, where the qubit frequencies are measured, the cable length is adjusted so that the cable mode is within $\pm \sim 1$ MHz of one qubit frequency, and then the control sequence is calibrated to maximize $\mathcal{F}_{\mathrm{RE}}$.

3. Quantum circuit simulations

Herein, we construct a quantum circuit model of proposed remote entanglement based on the results of time evolution simulations and perform quantum circuit simulations to compare computation using remote entanglement and in-node computation. We demonstrate that the proposed remote entanglement, which exhibits lower fidelity than in-node computation in teleportation of a physical qubit, can achieve nearly the same fidelity as in-node computation in logical qubit teleportation with through ingenuity in qubit arrangements and quantum circuits.

3.1. Simulation methods

For numerical simulations, we explicitly treat quantum state vector and consider amplitude and phase dampings for qubits [60, 61]. The amplitude and phase dampings are expressed by the following equations:

$$\begin{aligned} &\rho \rightarrow E_1^{\mathrm{AD}} \rho E_1^{\mathrm{AD}\dagger} + E_2^{\mathrm{AD}} \rho E_2^{\mathrm{AD}\dagger} \\ &E_1^{\mathrm{AD}} = \begin{pmatrix} 1 & 0 \\ 0 & \sqrt{1-p_{\mathrm{AD}}} \end{pmatrix}, E_2^{AD} = \begin{pmatrix} 0 & p_{\mathrm{AD}} \\ 0 & 0 \end{pmatrix}, \end{aligned} \tag{8}$$

$$\rho \to E_1^{\mathrm{PD}} \rho E_1^{\mathrm{PD}\dagger} + E_2^{\mathrm{PD}} \rho E_2^{\mathrm{PD}\dagger}$$
$$E_1^{\mathrm{PD}} = \begin{pmatrix} 1 & 0 \\ 0 & \sqrt{1-p_{\mathrm{PD}}} \end{pmatrix}, E_2^{\mathrm{PD}} = \begin{pmatrix} 0 & 0 \\ 0 & p_{\mathrm{PD}} \end{pmatrix}, \quad (9)$$

where AD and PD stand for amplitude and phase dampings, respectively, p_{AD} and p_{PD} are related to the relaxation times of qubits T_1 and T_2 and each operation time t by the following equation:

$$e^{-t/T_1} = 1 - -p_{\mathrm{AD}}$$
$$e^{-t/T_2} = \sqrt{1-p_{\mathrm{AD}}}\sqrt{1-p_{\mathrm{PD}}} \quad . \quad (10)$$

In this section, we use T_1 in the range of 100–500 μs and set $T_2 = T_1$ for simplicity. The operation times are set to $t = 20$ ns for one-qubit gates and $t = 200$ ns for two-qubit gates and measurements. All these parameters are typical values for fixed-frequency qubits.

For a teleportation of a logical qubit, after the teleportation, quantum error correction [60, 61] is performed once. Quantum error correction is performed by preparing a look-up table for syndrome. Auxiliary qubit errors can occur during quantum circuit execution; however, since the quantum error correction is performed only once, the error of the auxiliary qubit cannot be determined.

3.2. Quantum circuit model of remote entanglement

Herein, we construct a quantum circuit model of proposed remote entanglement (figure 1(d)) for use in quantum circuit simulations. The rate of state transfer P and error rates for qubit $p_{\mathrm{A}}^{\mathrm{AD}}$ and $p_{\mathrm{B}}^{\mathrm{AD}}$ for the model are determined to reproduce the density matrix of time evolution simulations of the Hamiltonian in equation (4) with dissipation, i.e. the Lindblad master equation in equation (5). The relaxation times of each transmission path mode T_m are presented in table 1 for both 1- and 0.25 m cables. The relaxation times of qubits are $T_1 = 100$, 200, 300, 400, and 500 μs. After a half-quantum state transfer and a subsequent rotation gate $R_Z(\theta)$ for correcting the phase shift, the state fidelity $\mathcal{F}_{\mathrm{RE}}$ to the ideal final state $\left|\Phi_{\mathrm{RE}}^{\mathrm{F}}\right\rangle$ is calculated.

The maximum $\mathcal{F}_{\mathrm{RE}}$, qubit frequency detuning $\Delta_{\mathrm{A}}/(2\pi)$, and control sequence parameters $\Delta\tau$, τ_{A}, τ, and θ are summarized in appendix B, table 2. The results do not depend significantly on T_1 because T_M of $\sim$10μs for a 1 m cable and $\sim$40μs for a 0.25 m cable are much smaller than T_1. The maximum $\mathcal{F}_{\mathrm{RE}}$ is 99.4%–99.5% at $\tau = 66.7$ ns for a 1 m cable and 99.9% at $\tau = 62.4$–62.5 ns for a 0.25 m cable. The difference in $\mathcal{F}_{\mathrm{RE}}$ between cable lengths of 1 and 0.25 m is considered to reflect the dependence of ω_{FSR} and T_m on cable length.

The model parameters P, $p_{\mathrm{AD}}^{\mathrm{A}}$, and $p_{\mathrm{AD}}^{\mathrm{B}}$ determined based on the time evolution simulations are also summarized in appendix B, table 2, where P and p_{AD} are 0.510–0.513 and 0.005–0.006 for a 1 m cable and 0.502 and 0.001 for a 0.25 m cable. Although P does not depend on T_1, error rates $p_{\mathrm{AD}}^{\mathrm{A}}$ and $p_{\mathrm{AD}}^{\mathrm{B}}$ gradually decrease according to T_1. This model enables us to incorporate the operation through transmission path with multi-dissipative modes into quantum circuit simulations. The phase damping of $T_2 = T_1$ for $t = \tau$ is separately executed in quantum circuit simulations.

3.3. Numerical simulations

3.3.1. Teleportation of a physical qubit

As an example of computation using remote entanglement, we first consider teleportation of a physical qubit (figure 1(e)). Any state is passed to another qubit by XX measurement and subsequent one-qubit operations. The teleportation of a physical qubit is performed using three qubits in a node or four qubits through a transmission path, which are referred to N3 and T4, respectively. The figure is the number of qubits, and N and T represent the computations in a node and through a transmission path, respectively. The corresponding quantum circuits are shown in appendix C, figure 13. The two-qubit XX measurement through a transmission path is executed using a logical auxiliary qubit scheme [62]. The simultaneous X measurements of the two entangled qubits correspond to XX measurement.

In numerical simulations, quantum state vectors are explicitly treated. The initial state $\left(\alpha\left|0^{\mathrm{A}}\right\rangle + \beta\left|1^{\mathrm{A}}\right\rangle\right) \otimes \left|0^{\mathrm{B}}\right\rangle$ is prepared, and operations in quantum circuits are applied in sequence. After each gate operation, amplitude and phase dampings are performed with the probability determined by the gate time and T_1. For the measurement, dampings are performed before the operation [61]. The half-quantum state transfer represented by ST/2 in the T4-quantum circuit is replaced by a remote entanglement model determined above. A state fidelity to $\alpha\left|0^{\mathrm{B}}\right\rangle + \beta\left|1^{\mathrm{B}}\right\rangle$ is calculated after teleportation. Each state fidelity is obtained by performing 1000 shots of the same calculation with different random numbers. We average 1000 fidelities consisting of 10 for each 100 random initial logical states (α and β).

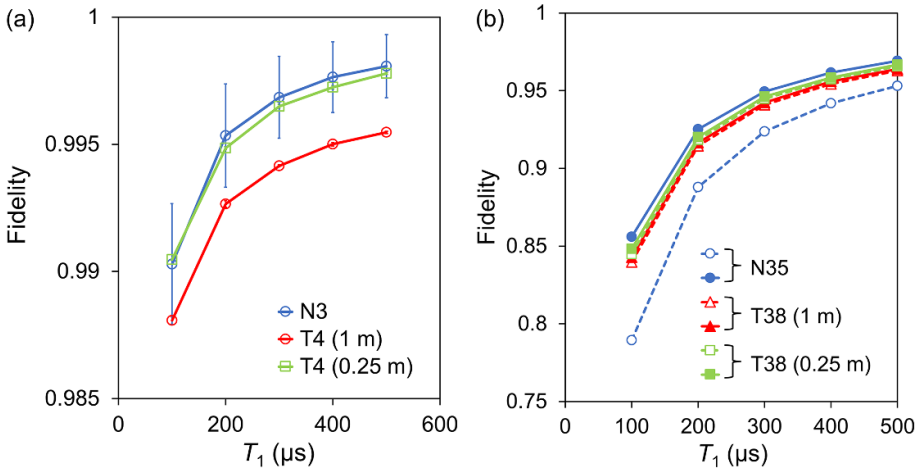

Figure 7. Numerical results of quantum circuit simulations for teleportation of (a) a physical qubit (N3 and T4) and (b) a logical qubit (N35 and T38), where the figure is the number of qubits, and N and T represent the computations in a node and through a transmission path, respectively. Average state fidelities are plotted as functions of the relaxation time of qubits T_1. For T-configuration, two cases have the coaxial cable length for the transmission path of 1 and 0.25 m. For (a), the error bars represent the respective standard deviations. For (b), the open and close symbols represent the fidelities immediately after teleportation and subsequent quantum error correction, respectively.

The numerical simulation results with N3- and T4-quantum circuits are shown in figure 7(a). The fidelity for N3-quantum circuit decreases as T_1 decreases. While the fidelities for T4-quantum circuit with a 0.25 m cable are nearly the same as those for N3-quantum circuit, the fidelities for T4-quantum circuit with a 1 m cable are lower than those for N3-quantum circuit. We find that the fidelities at $T_1 = 500$ μs reflect the fidelities of remote entanglement $\mathcal{F}_{\mathrm{RE}}$ presented in appendix B, table 2. As shown in figure 7(a), the standard deviation is $\sim$0.1 for N3-quantum circuit. For T4-quantum circuits, the standard deviations are much smaller and the error bars are shown within the symbols. This can be due to the qubit states and short time that the states are entangled in T4-quantum circuits.

3.3.2. Teleportation of a logical qubit

Next, we consider teleportation of a logical qubit with 3 $\times$ 3 surface codes [27, 63–71]. Figure 1(e) for teleportation of a physical qubit must be read as a logical qubit. Any logical state is passed to another logical qubit by $X_{\mathrm{L}}X_{\mathrm{L}}$ measurement and subsequent local logical operations, where the subscript 'L' means logical. We adopt lattice surgery [70–73] or its extension using remote entanglement for the operation between logical qubits, that is, $X_{\mathrm{L}}X_{\mathrm{L}}$ measurement. Figure 8 presents two types of qubit arrangements of two logical qubits, and the corresponding quantum circuits for teleportation of a logical qubit are shown in appendix C, figure 14.

Figure 8(a) is a 3 $\times$ 6 surface code for in-node computation, and the $X_{\mathrm{L}}X_{\mathrm{L}}$ measurement is realized by lattice surgery, that is, merging (two X measurements on the boundary of two logical qubits) and subsequent splitting (one-side Z measurement on the boundary of two logical qubits). A quantum circuit that simply replace two X measurements with those using remote entanglement suffers from a lower fidelity because extra operations are just added. Considering the transmission paths are formed at the edges of a qubit chip, we propose adding two extra auxiliary qubits to each logical qubit to reduce the number of quantum state transfers and shorten computational time. In figure 8(b), two logical qubits are connected by a transmission path. The two-logical qubit measurement $X_{\mathrm{L}}X_{\mathrm{L}}$ is executed using a logical auxiliary qubit scheme [62]. The six qubits between the two logical qubits are entangled through remote entanglement. The simultaneous X measurements of the six auxiliary qubits correspond to $X_{\mathrm{L}}X_{\mathrm{L}}$ measurement, which does not require splitting such as in-node computation. The qubit arrangements in figures 8(a) and (b) are referred to N35 and T38, respectively. The figure is the number of qubits, and N and T represent the computations in a node and through a transmission path, respectively. The total circuit time of T38-quantum circuit is shorter than that of N35-quantum circuit, thanks to the extra auxiliary qubits and a logical auxiliary qubit scheme. Both qubit configurations can be arranged with 64 qubits in a square lattice and tested experimentally.

Quantum circuits for teleportation of a logical qubit, where any logical state $\alpha|0_{\mathrm{L}}\rangle + \beta|1_{\mathrm{L}}\rangle$ is teleported from logical qubit A to B, are presented in appendix C, figure 14 for N35- and T38-configurations. In numerical simulations, quantum error correction of a 3 $\times$ 3 surface code [60, 61] is performed on logical

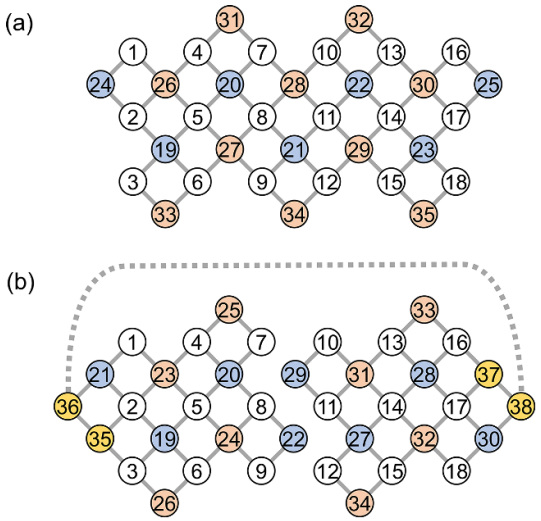

Figure 8. Qubit arrangements for teleportation of a logical qubit with 3 × 3 surface codes: (a) N35 and (b) T38, where the figure is the number of qubits, and N and T represent the computations in a node and through a transmission path, respectively. The white, red, blue, and orange circles represent the data, *X* measurement auxiliary, *Z* measurement auxiliary, and extra auxiliary qubits, respectively. The dashed curve indicates a transmission path.

qubit B after the teleportation. Quantum state vectors are explicitly treated. The initial state $\left(\alpha\left|0_{\mathrm{L}}^{\mathrm{A}}\right\rangle+\beta\left|1_{\mathrm{L}}^{\mathrm{A}}\right\rangle\right)\otimes\left|0_{\mathrm{L}}^{\mathrm{B}}\right\rangle$ is prepared, and operations in quantum circuits are applied in sequence. After each gate operation, amplitude and phase dampings are performed with the probability determined by the gate time and T_1. For the measurement, dampings are performed before the operation [61]. The half-quantum state transfer represented by ST/2 in the T38-quantum circuit is replaced by a remote entanglement model determined above. A state fidelity to $\alpha|0_{\mathrm{L}}^{\mathrm{B}}\rangle+\ \beta|1_{\mathrm{L}}^{\mathrm{B}}\rangle$ is calculated immediately after teleportation and after subsequent quantum error correction. Each state fidelity is obtained by performing 1000 shots of the same calculation with different random numbers. Averaging 1000 fidelities consisting of 10 for each 100 random initial logical states (α and β) yields an average fidelity with a standard deviation of $\sim$1%. These calculations require parallel computation with large memory. We use supercomputer systems for the quantum circuit simulations.

The numerical simulation results with N35- and T38-configurations are shown in figure 7(b). As can be seen in figures 7(a) and (b), the fidelities for teleportation of a physical qubit are much higher than those of a logical qubit, and the encoding is not meaningful at these T_1 and computational sizes from the viewpoint of protecting quantum information. However, in this study, we focus on comparing computations through remote entanglement and in-node computations in logical qubit operations for future fault tolerant quantum computing. The fidelity just after teleportation for N35-configuration is remarkably low. This is considered due to merging and splitting operations, where errors are likely to propagate, and long circuit times (1900 ns). However, quantum error correction works well, and the fidelity after error correction with N35-configurarion becomes the highest. The fidelities for T38-configuration are nearly the same as that after quantum error correction with N35-configuration. Fidelities immediately after teleportation do not decrease significantly. A short-circuit time of 1366.7 ns for a 1 m cable and 1362.4 ns for a 0.25 m cable and a logical auxiliary qubit scheme can contribute to this property. The fidelities, which decrease slightly with cable length, are considered to reflect the difference in $\mathcal{F}_{\mathrm{RE}}$ and therefore the dependence of ω_{FSR} and T_m on the cable length. These results show that the ingenuity in qubit arrangements and quantum circuits enables teleportation of a logic qubit with 3 × 3 surface codes even with a cable length of 1 m with a fidelity that is not significantly compromised from in-node computation.

4. Conclusion

We have characterized transmission paths with 1- or 0.25 m superconducting coaxial cables. Through time evolution simulations based on the characteristics, we have proposed remote entanglement with a high fidelity $>$ 99% even in the presence of a qubit frequency detuning. In the scheme, the standing-wave mode of the transmission path is set within $\pm\sim$ 1 MHz of either qubit frequency. The maximum fidelity with

dissipation is expected to be 99.4% for a 1 m cable and 99.8% for a 0.25 m cable with both qubit frequency detunings of 5 and 10 MHz. These results show the high adjustment capability of our scheme in remote entanglement operations, which sharply contrasts quantum state transfer where a qubit frequency detuning of 5 MHz substantially reduces the maximum fidelity. A quantum circuit model constructed based on time evolution simulations enables us to incorporate remote entanglement into quantum circuit simulations. Quantum circuit simulations have revealed that teleportation of a logical qubit with 3×3 surface codes, as an example of computation using remote entanglement that can be tried with current resources, is possible with a fidelity that is not significantly compromised from in-node computation even for a cable length of 1 m. The high-fidelity remote entanglement is promising not only for scaling up quantum computer systems but also for nonlocal connections on a qubit chip and thus non-2D quantum error-correcting codes.

Data availability statement

All data that support the findings of this study are included within the article (and any supplementary files).

Acknowledgment

We thank the Research Institute for Information Technology, Kyusyu University, and the Information Collaboration Promotion Headquarters, Nagoya University, for providing access to the supercomputer system for performing the calculations in this study.

Appendix A. Results of time evolution simulations for a 0.25 m cable

We have presented the results of time evolution simulations of quantum state transfer and remote entanglement for a transmission path with a 1 m cable in the main text. Here, we present the results for a 0.25 m cable, which is similar to the results for a 1 m cable.

Figure 9 shows the results of quantum state transfer without a qubit frequency detuning. For the state fidelity $\mathcal{F}_{\mathrm{ST}}$ without dissipation (blue solid curve), the second maximum $\mathcal{F}_{\mathrm{ST}}$ with respect $\Delta\tau$ is slightly higher than the first one; however, both maximum $\mathcal{F}_{\mathrm{ST}}$ become equal by dissipation (red-dotted curve) due to the longer control sequence duration for the second maximum. For large $\Delta\tau$, oscillations of approximately 2.5 ns correspond to $\omega_{\mathrm{FSR}}/(2\pi) = 0.3846$ GHz.

Figure 10 shows the results of quantum state transfer with a qubit frequency detuning. A qubit frequency detuning $\Delta/(2\pi)$ of 5 MHz substantially reduces $\mathcal{F}_{\mathrm{ST}}$, and the high fidelity for each $\Delta\tau$ is obtained when the standing-wave mode is near the center for the qubit frequency detuning of 5 MHz, as in the case for a 1 m cable.

Figure 11 shows the results of remote entanglement without a qubit frequency detuning. The state fidelity $\mathcal{F}_{\mathrm{RE}}$ without dissipation (blue solid curve) is approximately along the concurrence C (orange-dashed curve), which means that the phase of the qubit $|01\rangle$ state relative to the $|10\rangle$ state does not change during the state transfer. The state fidelity $\mathcal{F}_{\mathrm{RE}}$ is as high as 99.98% without dissipation and 99.90% with dissipation.

Figure 12 shows the results of remote entanglement with a qubit frequency detuning $\Delta/(2\pi)$ of 5 MHz. After correcting phase shift with a rotation gate $R_Z(\theta)$, the state fidelity $\mathcal{F}_{\mathrm{RE}}$ without dissipation (blue solid curve) is approximately along the concurrence C (orange-dashed curve). The maximum $\mathcal{F}_{\mathrm{RE}}$ is as high as 99.96% without dissipation and 99.88% with dissipation. This sharply contrasts quantum state transfer where a detuning of 5 MHz substantially reduces the maximum $\mathcal{F}_{\mathrm{ST}}$ value.

Except for quantum state transfer in the presence of a qubit frequency detuning, the state fidelity for a 0.25 m cable is higher than that of a 1 m cable. This is considered due to the larger ω_{FSR} and long relaxation times T_m. The fidelity for quantum state transfer with a qubit frequency detuning is as low as that with a 1 m cable because the cause is not related to ω_{FSR}.

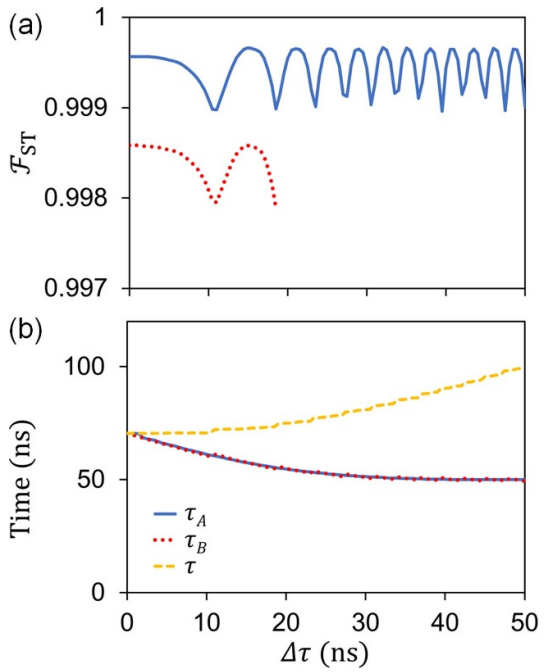

Figure 9. Results of time evolution simulations of quantum state transfer without a qubit frequency detuning for a 0.25 m coaxial cable. The first and second maximum $\mathcal{F}_{ST}$ (%) and the control sequence parameters $\Delta\tau$, τ_A, and τ (ns) are summarized as $\{\mathcal{F}_{ST}, \Delta\tau, \tau_A, \tau\} = \{99.96, 0.0, 70.5, 70.5\}$ and $\{99.97, 15.0, 57.6, 72.6\}$ without dissipation and $\{99.86, 0.0, 70.5, 70.5\}$ and $\{99.86, 14.9, 57.7, 72.6\}$ with dissipation. Other explanations are the same as those in figure 2.

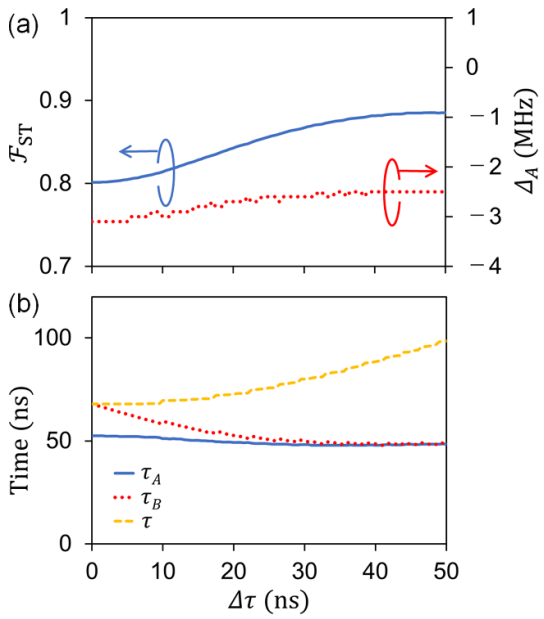

Figure 10. Results of time evolution simulations of quantum state transfer with a qubit frequency detuning of 5 MHz for a 0.25 m coaxial cable without dissipation. The maximum $\mathcal{F}_{ST}$ (%), the control sequence parameters $\Delta\tau$, τ_A, and τ (ns), and $\Delta_A/(2\pi)$ (MHz) are summarized as $\{\mathcal{F}_{ST}, \Delta\tau, \tau_A, \tau, \Delta_A/(2\pi)\} = \{88.56, 50.0, 48.5, 98.5, -2.5\}$. Other explanations are the same as those in figure 3.

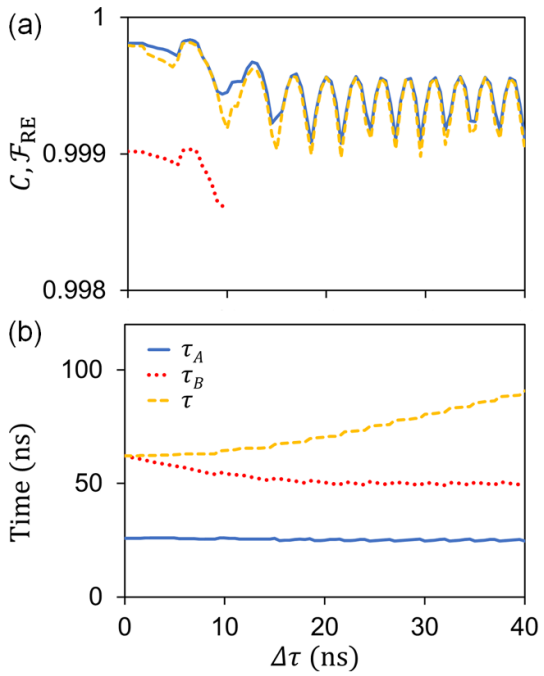

Figure 11. Results of time evolution simulations of remote entanglement without a qubit frequency detuning for a 0.25 m coaxial cable. The first and second maximum $\mathcal{F}_{RE}$ (%) and the control sequence parameters $\Delta\tau$, τ_A, and τ (ns) are summarized as $\{\mathcal{F}_{RE}, \Delta\tau, \tau_A, \tau\} = \{99.98, 1.0, 25.9, 62,2\}$ and $\{99.98, 6.3, 25.7, 63.0\}$ without dissipation and $\{99.90, 0.9, 25.9, 62.2\}$ and $\{99.90, 6.0, 25.7, 63.0\}$ with dissipation. Other explanations are the same as those in figure 4.

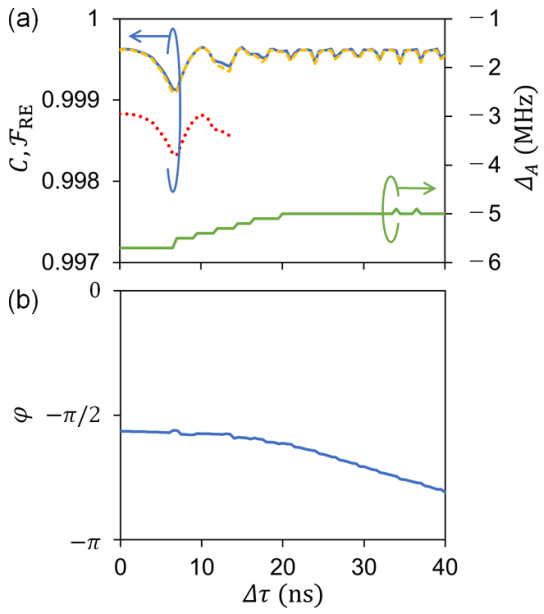

Figure 12. Results of time evolution simulations of remote entanglement with a qubit frequency detuning of 5 MHz for a 0.25 m coaxial cable. The first and second maximum $\mathcal{F}_{RE}$ (%), control sequence parameters $\Delta\tau$, $\tau_A/(2\pi)$, and τ (ns), $\Delta_A/(2\pi)$ (MHz), and θ for $R_z(\theta)$ are summarized as $\{\mathcal{F}_{RE}, \Delta\tau, \tau_A/(2\pi), \tau, \Delta_A, \theta\} = \{99.96, 1.0, 27.2, 62.4, -5.7, 0.56\pi\}$ and $\{99.96, 10.1, 26.6, 64.5, -5.4, 0.57\pi\}$ without dissipation and $\{99.88, 1.0, 27.2, 62.4, -5.7, 0.56\pi\}$ and $\{99.88, 9.9, 26.6, 64.5, -5.4, 0.57\pi\}$ with dissipation. Other explanations are the same as those in figure 5.

Appendix B. Quantum circuit model of remote entanglement

The schematic of a quantum circuit model of remote entanglement is illustrated in figure 1(d). The models are constructed based on time evolution simulations with dissipation. The maximum $\mathcal{F}_{RE}$, control sequence parameters for $T_1 = 100$, 200, 300, 400, and 500 μs, are summarized in table 2. The model parameters P, p^A_{AD}, and p^B_{AD}, which are also summarized in table 2, are determined to reproduce the density matrix for the time evolution simulations.

Table 2. Results of time evolution simulations for remote entanglement with dissipation ($\mathcal{F}_{\rm RE}$, $\Delta_{\rm A}/(2\pi)$, $\Delta\tau$, $\tau_{\rm A}$, τ, and θ). The target cable lengths are 1 and 0.25 m. The corresponding rate of state transfer (P) and error rates for amplitude damping ($p^{\rm A}_{\rm AD}$ and $p^{\rm B}_{\rm AD}$) for a quantum circuit model of remote entanglement shown in figure 1(d) are included.

Cable Length	T_1 (μs)	100	200	300	400	500
1 m	$\mathcal{F}_{\rm RE}$	99.44	99.36	99.47	99.48	99.48
	$\Delta_{\rm A}/(2\pi)$ (MHz)	−5.2	−5.2	−5.2	−5.2	−5.2
	$\Delta\tau$ (ns)	14.3	14.2	14.2	14.2	14.4
	$\tau_{\rm A}$ (ns)	26.7	26.8	26.7	26.8	26.7
	τ (ns)	66.7	66.7	66.7	66.7	66.7
	θ (π)	0.58	0.58	0.58	0.58	0.58
	P	0.5101	0.5127	0.51	0.5128	0.5102
	$p^{\rm A}_{\rm AD}$	0.0055	0.0052	0.0052	0.0051	0.0051
	$p^{\rm B}_{\rm AD}$	0.0056	0.0052	0.0052	0.0051	0.0051
0.25 m	$\mathcal{F}_{\rm RE}$	99.88	99.91	99.91	99.92	99.92
	$\Delta_{\rm A}/(2\pi)$ (MHz)	−5.7	−5.7	−5.7	−5.7	−5.7
	$\Delta\tau$ (ns)	1.0	0.9	1.1	1.1	1.1
	$\tau_{\rm A}$ (ns)	27.2	27.2	27.2	27.2	27.2
	τ (ns)	62.4	62.4	62.5	62.4	62.4
	θ (π)	0.56	0.56	0.56	0.56	0.56
	P	0.5015	0.5015	0.5015	0.5015	0.5015
	$p^{\rm A}_{\rm AD}$	0.0011	0.0009	0.0008	0.0008	0.0007
	$p^{\rm B}_{\rm AD}$	0.0012	0.0009	0.0009	0.0008	0.0008

Appendix C. Quantum circuits for teleportation of physical and logical qubits

A schematic of a quantum circuit for teleportation of a physical qubit is presented in figure 1(e). Figures 13(a) and (b) show quantum circuits for teleportation in a node (N3) and through remote entangelement (T4), respectively. For the T4-quantum circuit, two qubits are connected by a transmission path. The symbol ST/2 represents half-quantum state transfer, that is, remote entanglement. The simultaneous X measurements of the two entangled auxiliary qubits (steps 4–6) correspond to the XX measurement.

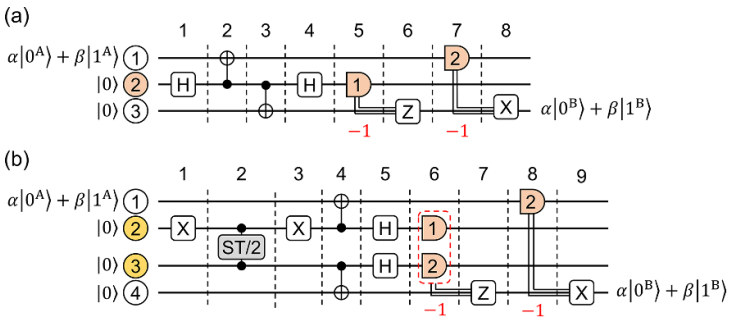

Figure 13. Quantum circuits for teleportation of a physical qubit (a) in a node and (b) through remote entanglement. The symbol ST/2 represents half-quantum state transfer. The semi-oval shape represents the measurement. The measurements enclosed by the dashed line determine the subsequent gate operations depending on the product of the measurement results. The total circuit time is 880 ns for (a) and 766.7 and 762.4 ns for (b) with 1- and 0.25 m cables, respectively.

Figure 1(e) for teleportation of a physical qubit must be read as a logical qubit. Quantum circuits can be written as shown in figures 14(a) and (b) for the N35- and T38-qubit arrangements (figure 8), respectively. The N35-qubit arrangement is a 3 × 6 surface code, and the $X_{\rm L}X_{\rm L}$ measurement is realized by merging (steps 1–8 in figure 14(a)) and subsequent splitting (steps 9–14). For the T38-qubit arrangement, two logical qubits are connected by a transmission path. The symbol ST/2 represents half-quantum state transfer, that is, remote entanglement. The six qubits between the two logical qubits are entangled through remote entanglement (steps 1–7 in figure 14(b)). The simultaneous X measurements of the six auxiliary qubits (steps 8–10) correspond to the $X_{\rm L}X_{\rm L}$ measurement, which does not require splitting such as the N35-quantum circuit. This leads to short-circuit times for the T-38 quantum circuit of 1366.7 ns for a 1 m cable and 1362.4 ns for a 0.25 m cable, compared with 1900 ns for the N35-quantum circuit.

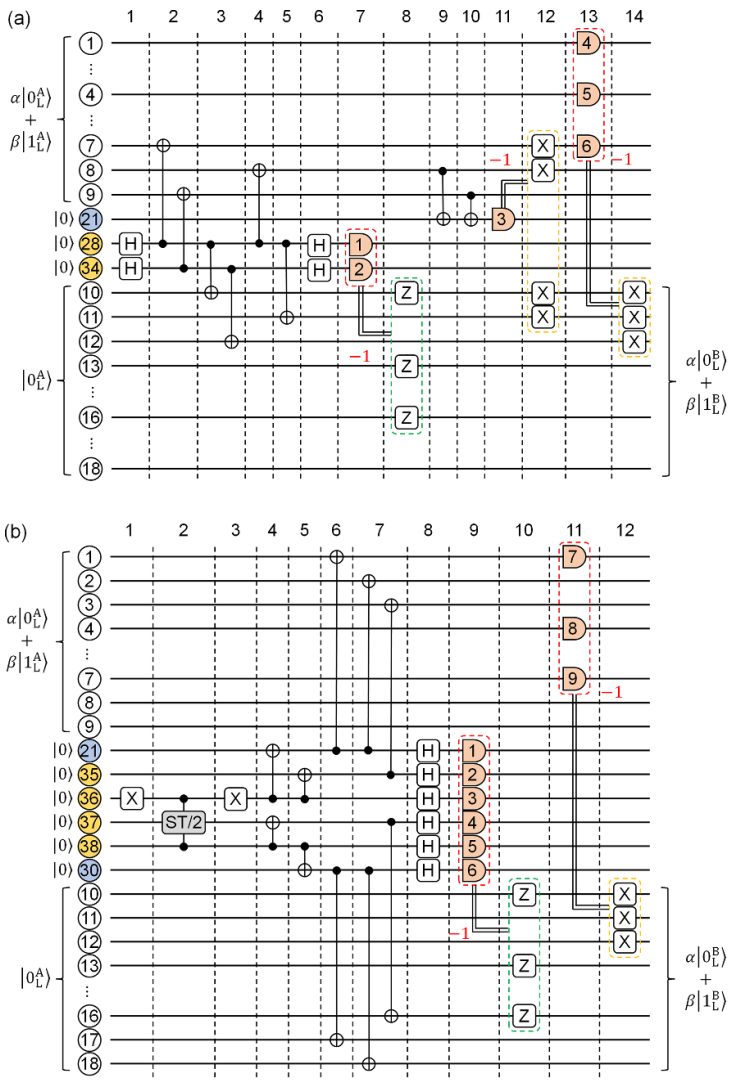

Figure 14. Quantum circuits for teleportation of a logical qubit based on the (a) N35- and (b) T38-qubit arrangements. The subscript 'L' means logical. The symbol ST/2 represents half-quantum state transfer. The semi-oval shape represents the measurement. The measurements enclosed by the dashed line determine the subsequent gate operations depending on the product of the measurement results. The total circuit time is 1900 ns for the N35-quantum circuit and 1366.7 and 1362.4 ns for the T38-quantum circuit with 1- and 0.25 m cables, respectively.

In numerical simulations, after each gate operation, amplitude and phase dampings are performed. For the measurement, dampings are performed before the operation. The half-quantum state transfer represented by ST/2 in the T-quantum circuits is replaced by the quantum circuit model of remote entanglement determined based on the time evolution simulations. For logical qubit teleportation, quantum error correction of a 3 $\times$ 3 surface code is executed on logical qubit B after N35- an T38-quantum circuits.

ORCID iD

Mari Ohfuchi https://orcid.org/0000-0001-6360-5726

References

[1] Byrd G T and Ding Y 2023 *Computer* **56** 20–29
[2] Bravyi S, Dial O, Gambetta J M, Gil D and Nazario Z 2022 *J. Appl. Phys.* **132** 160902
[3] Awschalom D *et al* 2021 *PRX Quantum* **2** 017002
[4] Gold A *et al* 2021 *npj Quantum Inf.* **7** 142
[5] Marxer F *et al* 2023 *PRX Quantum* **4** 010314
[6] Zhong Y *et al* 2021 *Nature* **590** 571–5
[7] Niu J *et al* 2023 *Nat. Elecron.* **6** 235–41
[8] Leung N, Lu Y, Chakram S, Naik R K, Earnest N, Ma R, Jacobs K, Cleland A N and Schuster D I 2019 *npj Quantum Inf.* **5** 18

[9] Zhong Y P *et al* 2019 *Nat. Phys.* **15** 741–4
[10] Cirac J I, Zoller P, Kimble H J and Mabuchi H 1997 *Phys. Rev. Lett.* **78** 3221–4
[11] Kurpiers P *et al* 2018 *Nature* **558** 264–7
[12] Axline C J *et al* 2018 *Nat. Phys.* **14** 705–10
[13] Campagne-Ibarcq P *et al* 2018 *Phys. Rev. Lett.* **120** 200501
[14] Magnard P *et al* 2020 *Phys. Rev. Lett.* **125** 260502
[15] Chang H-S *et al* 2020 *Phys. Rev. Lett.* **124** 240502
[16] Burkhart L D, Teoh J D, Zhang Y, Axline C J, Frunzio L, Devoret M, Jiang L, Girvin S and Schoelkopf R 2021 *PRX Quantum* **2** 030321
[17] Pechal M and Safavi-Naeini A H 2017 *Phys. Rev.* A **96** 042305
[18] Safavi-Naeini A H, Thourhout D V, Baets R and Laer R V 2019 *Optica* **6** 213–32
[19] Dumur E´*et al* 2021 *npj Quantum Inf.* **7** 173
[20] Mirhosseini M, Sipahigil A, Kalaee M and Painter O 2020 *Nature* **588** 599–603
[21] Han X, Fu W, Zou C-L, Jiang L and Tang H X 2021 *Optica* **8** 1050–64
[22] Hisatomi R, Osada A, Tabuchi Y, Ishikawa T, Noguchi A, Yamazaki R, Usami K and Nakamura Y 2016 *Phys. Rev.* B **93** 174427
[23] Hönl S, Popoff Y, Caimi D, Beccari A, Kippenberg T J and Seidler P 2022 *Nat. Commun.* **13** 2065
[24] Chiappina P, Banker J, Meesala S, Lake D, Wood S and Painter O 2023 *Opt. Express* **31** 22914–27
[25] Yin Y *et al* 2013 *Phys. Rev. Lett.* **110** 107001
[26] Storz S *et al* 2023 *Nature* **617** 265
[27] Campbell E T, Terhal B M and Vuillot C 2017 *Nature* **549** 172–9
[28] Barends R *et al* 2014 *Nature* **508** 500–3
[29] DiCarlo L *et al* 2009 *Nature* **460** 240–4
[30] Kelly J *et al* 2015 *Nature* **519** 66–69
[31] Reagor M *et al* 2018 *Sci. Adv.* **4** eaao3603
[32] Chen Y *et al* 2014 *Phys. Rev. Lett.* **113** 220502
[33] Koch J, Yu T M, Gambetta J, Houck A A, Schuster D I, Majer J, Blais A, Devoret M H, Girvin S M and Schoelkopf R J 2007 *Phys. Rev.* A **76** 042319
[34] Allman M S *et al* 2014 *Phys. Rev. Lett.* **112** 123601
[35] Sirois A J, Castellanos-Beltran M A, DeFeo M P, Ranzani L, Lecocq F, Simmonds R W, Teufel J D and Aumentado J 2015 *Appl. Phys. Lett.* **106** 172603
[36] Axline C, Reagor M, Heeres R, Reinhold P, Wang C, Shain K, Pfaff W, Chu Y, Frunzio L and Schoelkopf R J 2016 *Appl. Phys. Lett.* **109** 042601
[37] Reagor M *et al* 2016 *Phys. Rev.* B **94** 014506
[38] McKay D C, Filipp S, Mezzacapo A, Magesan E, Chow J M and Gambetta J M 2016 *Phys. Rev. Appl.* **6** 064007
[39] Lu Y, Chakram S, Leung N, Earnest N, Naik R K, Huang Z, Groszkowski P, Kapit E, Koch J and Schuster D I 2017 *Phys. Rev. Lett.* **119** 150502
[40] Jurcevic P *et al* 2021 *Quantum Sci. Technol.* **6** 025020
[41] Place A P M *et al* 2021 *Nat. Commun.* **12** 1779
[42] Rigetti C and Devoret M 2010 *Phys. Rev.* B **81** 134507
[43] de Groot P C, Lisenfeld J, Schouten R N, Ashhab S, Lupaşcu A, Harmans C J P M and Mooij J E 2010 *Nat. Phys.* **6** 763
[44] Chow J M *et al* 2011 *Phys. Rev. Lett.* **107** 080502
[45] de Groot P C, Ashhab S, Lupaşcu A, DiCarlo L, Nori F, Harmans C J P M and Mooij J E 2012 *New J. Phys.* **14** 073038
[46] Córcoles A D, Gambetta J M, Chow J M, Smolin J A, Ware M, Strand J, Plourde B L T and Steffen M 2013 *Phys. Rev.* A **87** 030301
[47] Sheldon S, Magesan E, Chow J M and Gambetta J M 2016 *Phys. Rev.* A **93** 060302
[48] Patterson A *et al* 2019 *Phys. Rev. Appl.* **12** 064013
[49] Sundaresan N, Lauer I, Pritchett E, Magesan E, Jurcevic P and Gambetta J M 2020 *PRX Quantum* **1** 020318
[50] Kandala A, Wei K X, Srinivasan S, Magesan E, Carnevale S, Keefe G A, Klaus D, Dial O and McKay D C 2021 *Phys. Rev. Lett.* **127** 130501
[51] Heya K and Kanazawa N 2021 *PRX Quantum* **2** 040336
[52] Malekakhlagh M and Magesan E 2022 *Phys. Rev.* A **105** 012602
[53] Hertzberg J B *et al* 2021 *npj Quantum Inf.* **7** 129
[54] Zhang E J *et al* 2022 *Sci. Adv.* **8** eabi6690
[55] Ohfuchi M and Sato S 2024 *Quantum Sci. Technol.* **9** 035014
[56] Sundaresan N M *et al* 2015 *Phys. Rev.* X **5** 021035
[57] Johansson J, Nation P and Nori F 2012 *Comput. Phys. Commun.* **183** 1760–72
[58] Johansson J, Nation P and Nori F 2013 *Comput. Phys. Commun.* **184** 1234
[59] Wootters W K 1998 *Phys. Rev. Lett.* **80** 2245
[60] Acharya R *et al* (Google Quantum AI) 2023 *Nature* **614** 676–68
[61] Tomita Y and Svore K M 2014 *Phys. Rev.* A **90** 062320
[62] Lao L and Almudever C G 2020 *Phys. Rev.* A **101** 032333
[63] Bravyi S B and Kitaev A Y 1998 (arXiv:quant-ph/9811052)
[64] Dennis E, Kitaev A, Landahl A and Preskill J 2002 *J. Math. Phys.* **43** 4452–505
[65] Kitaev A Y 2003 *Ann. Phys.* **303** 2–30
[66] Raussendorf R and Harrington J 2007 *Phys. Rev. Lett.* **98** 190504
[67] Fowler A G, Mariantoni M, Martinis J M and Cleland A N 2012 *Phys. Rev.* A **86** 032324
[68] Zhao Y *et al* 2022 *Phys. Rev. Lett.* **129** 030501
[69] Krinner S *et al* 2022 *Nature* **605** 669
[70] Horsman D, Fowler A G, Devitt S and Van Meter R 2012 *New J. Phys.* **14** 123011
[71] Poulsen Nautrup H, Friis N and Briegel H 2017 *Nat. Commun.* **8** 1321
[72] Gutiérrez M, Müller M and Bermúdez A 2019 *Phys. Rev.* A **99** 022330
[73] Erhard A *et al* 2021 *Nature* **589** 220